Molecular Engineering of Organic–Inorganic Hybrid Perovskites Quantum Wells

Yao Gao[1], Enzheng Shi[1], Shibin Deng[2], Stephen B. Shiring[1], Jordan M. Snaider[2], Chao Liang[3], Biao Yuan[3], Ruyi Song[4], Svenja M. Janke[5], Alexander Liebman-Peláez[6,†], Pilsun Yoo[7], Matthias Zeller[2], Bryan W. Boudouris[1,2], Peilin Liao[7], Chenhui Zhu[6], Volker Blum[4,5], Yi Yu[3], Brett M. Savoie[1], Libai Huang[2], Letian Dou[1]*

[1]Charles D. Davidson School of Chemical Engineering, Purdue University, West Lafayette, Indiana 47907, United States. [2]Department of Chemistry, Purdue University, West Lafayette, Indiana 47907, United States. [3]School of Physical Science and Technology, ShanghaiTech University, Shanghai 201210, China. [4]Department of Chemistry, Duke University, Durham, North Carolina 27708, United States. [5]Department of Mechanical Engineering and Materials Science, Duke University, Durham, North Carolina 27708, United States. [6]Advanced Light Source, Lawrence Berkeley National Laboratory, Berkeley, California 94720, United States. [7]School of Materials Engineering, Purdue University, West Lafayette, Indiana 47907, United States. [†]Present address: Department of Physics, University of California, Berkeley, California 94720, United States.

*Corresponding author. E-mail: dou10@purdue.edu (L.D.)

Semiconductor quantum-well structures and superlattices are key building blocks in modern optoelectronics, but it is difficult to simultaneously realize defect-free epitaxial growth and fine-tuning of the chemical composition, layer thickness, and band structure of each layer to achieve the desired performance. Here, we demonstrate the modulation of the electronic structure, and consequently the optical properties, of organic semiconducting building blocks incorporated between the layers of perovskites through a facile solution-processing step. The self-aggregation of the conjugated organic molecules is suppressed by functionalization with sterically demanding groups, and single-crystalline organic-perovskite hybrid quantum wells (down to one-unit-cell thick) are obtained. The energy and charge transfers between adjacent organic and inorganic layers were shown to be fast and efficient, owing to the atomically flat interface and ultra-small interlayer distance of the perovskite materials. The resulting 2D hybrid perovskites are very stable, owing to the protection of the bulky hydrophobic organic groups.

Semiconductor quantum wells (heterostructures in which a thin layer of one semiconductor is sandwiched between two layers of a different semiconductor material) and superlattices are the foundation of many electronic and optoelectronic devices including light-emitting diodes (LED), lasers, infrared photodetectors, and thermoelectric devices[1-3]. Two-dimensional (2D) layered halide perovskites have attracted considerable attention as an alternative to III-V compounds for achieving quantum well structures due to their solution-processability, their wide structure and property tunability, and excellent optoelectronic properties[4-21]. 2D perovskite structures can be understood as atomically thin slabs cut from the 3D parent structures along different crystal directions that are sandwiched by two layers of large organic cations[22,23]. There has been a large number of reports in the 1990s regarding 2D perovskites that incorporate insulating aliphatic ammonium cations which showed increasing energy barriers with larger barrier heights. However, only sparse efforts have been made to incorporate semiconducting organic moieties to tune the overall electronic properties. Among the few examples are spin-casted thin films containing simple aromatic pyrene, di-acetylene, oligothiophene, and carbazole units[24-34]. In most attempts only polycrystalline thin films with low crystallinity were obtained, hindering a better understanding of the structures and properties of these materials. Notably, Mitzi *et al.*[26] and Mercier *et al.*[28] successfully grew several quaterthiophene-perovskite and bithiophene-perovskite hybrid crystals using di-ammonium cations and elucidated their structure-property relationships, respectively. Very recently, conjugated diynes and fused ring compounds are incorporated into perovskite crystals[35,36]. Common to all reports was that the incorporation of large conjugated organic groups into the inorganic matrix was found to be challenging. For instance, Mercier pointed out that the incorporation of mono-ammonium terminated bi-thiophene cations leads to a head to tail arrangement of the molecules and precludes the formation of 2D perovskite crystals[28].

To date, the range of organic cations that have been incorporated into the crystal lattice remains limited, and a fundamental grasp about how molecular structures influence the overall morphology and properties of the perovskites is still lacking. We believe that organic chemistry principles, to date underutilized, could play an important role in the design of high quality hybrid quantum well structures with tailored properties. Here, we demonstrate a robust molecular design strategy for the synthesis of a variety of organic-inorganic hybrid perovskite mono-quantum wells (down to one unit cell thick) and multiple quantum wells with tunable electronic properties and excellent stability.

Results and discussion

Synthesis and crystal structures of hybrid perovskites quantum wells

Fig.1a shows the chemical structures of the conjugated ligands that were synthesized. Asymmetric mono-ammonium cationic species were selected over symmetric di-ammonium cations in order to achieve better control over the surface chemistry (i.e., to ensure that the surface of crystals or monolayers is terminated by organic groups) and the crystal morphology (i.e., to enhance in-plane lateral growth and suppress out-of-plane growth). In addition, mono-ammonium cations are more hydrophobic, which helps to improve stability toward moisture. Besides the conjugated ligands, the widely used insulating butylammonium ligand (**BA**) was chosen for comparison. The shortest conjugated ligand we designed here is based on a bithiophene unit (**2T**). To extend the conjugation and reduce the band gap, a tetrathiophene ligand (**4T**) has been included. However, we observed strong intermolecular π-π interactions and very poor solubility of the mono-ammonium terminated **4T** ligand. To address this issue, we incorporated two sterically more demanding methyl groups to form a new ligand (**4Tm**) to suppress intermolecular self-aggregation and self-crystallization. Note that even larger steric groups may be used, but the overall width of the ligand should not exceed the perovskite lattice (Supplementary Information, SI, Supplementary Fig. 1). To fine-tune the electronic properties and band alignments with respect to the perovskite layer, we introduced two strongly electron-withdrawing cyano groups and a small band gap chromophore 2,1,3-benzothiadiazole unit to make two new ligands, **4TCNm** and **BTm**, respectively. The synthetic route towards the π-conjugated organic cations and related structural characterizations can be found in the SI.

Using simple solution phase crystallization methods, we successfully synthesized bulk crystals for four of the hybrid materials, namely $(BA)_2PbI_4$, $(2T)_2PbI_4$, $(4Tm)_2PbI_4$, and $(BTm)_2PbI_4$. Specifically, a DMF solution of the compound (0.2~0.3 M) was prepared and chloroform vapor was diffused into the DMF solution slowly. The crystal structures of the three new materials, $(2T)_2PbI_4$, $(4Tm)_2PbI_4$, and $(BTm)_2PbI_4$, were resolved using single-crystal X-ray diffraction (XRD) and the side view of the structures are shown in Fig. 1b-1e (for more structure details, see Supplementary Fig. 2-4 and Supplementary Tables 1-3; Structural data for reference material $(BA)_2PbI_4$ had been reported by Mitzi and by Billing and Lemmerer)[37,38]. We failed to obtain single crystals suitable for structure determination for $(4T)_2PbI_4$ because of strong self-aggregation and low solubility of the **4T** molecules. As shown in Supplementary Fig. 5, a more diluted solution of $(4T)_2PbI_4$ in DMF (0.1 M) is highly turbid, and it cannot be fully dissolved even at 100 °C. In contrast, $(4Tm)_2PbI_4$ readily dissolves in DMF (0.3 M) at room temperature. The strong π-π interactions and very low solubility of the **4T** molecule make it difficult to grow high quality perovskite type crystals. For $(4TCNm)_2PbI_4$ we also had been not able to obtain large-size crystals suitable for single-crystal X-ray diffraction analysis. In this case, no self-aggregation issue was observed. We note that **4TCNm** is the bulkiest ligand, which may be too close to the limit of the perovskite lattice (Supplementary Fig. 1). Oversize in the ligand width could also introduce significant steric hindrance preventing crystals to grow to large enough size for single crystal structural analysis. Nevertheless, powder XRD and grazing-incidence wide-angle X-ray scattering studies on polycrystalline samples indicate $(4TCNm)_2PbI_4$ has correct 2D layered structure (Supplementary Fig. 6 and 7).

The layer thicknesses for $(BA)_2PbI_4$, $(2T)_2PbI_4$, $(4Tm)_2PbI_4$, $(4TCNm)_2PbI_4$, and $(BTm)_2PbI_4$ 2D sheets were found to be 13.7, 20.3, 31.8, 35.2, and 33.8 Å, respectively. The basic structures of the compounds incorporating conjugated ligands are close to be being isotypic with that of $(BA)_2PbI_4$. In $(2T)_2PbI_4$ and $(BTm)_2PbI_4$ the monoclinic symmetry is broken, and instead triclinic modulated superstructures are formed. Note, in all structures the environment of the lead atoms is distorted from the ideal octahedral. The lead ion is displaced from the central position of the octahedron towards one of the apical iodine atoms, and away from the other. For example, apical Pb-I bond distances of 3.022(7) and 3.464(7) Å are found in $(4Tm)_2PbI_4$ (the equatorial Pb-I bonds are 3.137(2) Å).

The arrangements of the conjugated organic ligands are slightly different. For $(4Tm)_2PbI_4$ and $(BTm)_2PbI_4$, the inorganic layers and the first two thiophene units from the ammonium end are nearly superimposable (Supplementary Fig. 8) and distinct differences start to appear at the position of the benzothiadiazole unit of the **4TCNm** ligand and the third thiophene unit of the **4Tm** ligand. The ligands on both sides of the inorganic layer are related to each other by inversion, making these two structures centrosymmetric. This is different for $(2T)_2PbI_4$. The inorganic layers and the organic layers on one side do again match the arrangement in $(4Tm)_2PbI_4$ and $(BTm)_2PbI_4$. The **2T** ligands on both sides, however, are related to each other by an approximate two-fold rotation, rather than inversion, thus creating a non-centrosymemtric chiral arrangement. An overlay of all three structures is given in Supplementary Fig. 8. The loss of inversion symmetry may result in ferroelectricity in these materials[39]. It is also worth noting that the organic groups are in their lowest energy configurations. For example, the four thiophene rings in $(4Tm)_2PbI_4$ are all in the trans configuration, which is significantly different from the situation in the di-ammonium system reported earlier[26]. This is probably because the mono-ammonium ligands have more freedom to rotate; whereas for the di-ammonium ligands, the two ends are all ionically bonded to the inorganic layers and molecules are forced into energetically less favorable conformations and under “stress”.

Nanocrystals growth and optical properties

The new mono-ammonium terminated conjugated ligands can be used to grow molecularly-thin 2D crystals (down to a single quantum well thick) directly on Si/SiO_2 substrates from a ternary co-solvent[13]. Fig. 2a shows optical microscope images of the assembled 2D crystals of $(2T)_2PbI_4$, $(4Tm)_2PbI_4$, $(4TCNm)_2PbI_4$ and $(BTm)_2PbI_4$ and the images of the corresponding single quantum wells in the insets. 2D sheets with a lateral size of around 10 to 20 µm and well-defined square shapes were obtained. The thickness was characterized by atomic force microscopy (Supplementary Fig. 9). 2D crystals with thicknesses of 3~4 nm were confirmed, indicating a single quantum well structure with only one layer of the PbI_4^{2-} sheet sandwiched by two layers of the organic semiconducting ligands can be obtained. Supplementary Fig. 10 and 11 display low-dose filtered high-resolution transmission electron microscopy (TEM) images of the new ultrathin 2Ds crystal. Using this technique, we were able to observe the lattice fringes of the 2D sheet. The electron diffraction data also match well with the X-ray diffraction data. These results indicate that the single crystalline nature is retained for the molecularly-thin 2D crystals and further confirm that they all have similar crystal structures.

Fig. 2b shows the corresponding photoluminescence (PL) images under UV irradiation and Fig. 2c shows the PL spectra of the mono-layer sheets (red curve) and the bulk crystals (dark red curve) under a 375 nm laser. The PL and absorption spectra of the pure organic ligands are shown in Supplementary Fig. 12 and 13. For comparison, the PL spectrum of the previously reported 2D perovskite $(BA)_2PbI_4$ is also shown (the grey dashed curves). $(2T)_2PbI_4$ exhibits a green color, $(4Tm)_2PbI_4$ and $(4TCNm)_2PbI_4$ display no PL, and $(BTm)_2PbI_4$ shows a red color. A mono-layer $(2T)_2PbI_4$ crystal shows a strong and narrow green PL with a peak at 518.4 nm (full width at half maximum is 20 nm), which is very close to that of $(BA)_2PbI_4$, indicating that the PL originates from the inorganic layer. The PL of the $(2T)_2PbI_4$ mono-quantum well is about 7 nm blue-shifted compared to the bulk crystal (525.2 nm), which is likely due to structural relaxation of the soft lattice and variation in dielectric confinement[40,41]. Similar effects are observed in $(BA)_2PbI_4$ (Fig. 2c(i) inset) and other systems[13]. A bi-layer $(BTm)_2PbI_4$ crystal shows a strong red PL at ~660 nm, which is from the **BTm** ligands, while no PL from the inorganic layer is detected. The PL of the bi-layer is ~6 nm blue-shifted compared to the PL of the bulk crystal. The PL results of $(2T)_2PbI_4$ and $(BTm)_2PbI_4$ are consistent with a type I heterojunction and energy transfers efficiently to the lowest energy emitter. For $(4Tm)_2PbI_4$ and $(4TCNm)_2PbI_4$, emissions from both the inorganic layer and the organic layers are 99.9% quenched (Fig. 2c(ii) and 2c(iii) insets), suggesting efficient charge separation at the interface[42].

Band alignments and charge carrier dynamics

To better clarify the band alignments, ultraviolet photoelectron spectroscopy (UPS) and cyclic voltammetry (CV) were employed (Supplementary Table 4). The valence band maximums (VBM) of $(BA)_2PbI_4$ was determined to be ~-5.89 eV. We assume a similar value for the PbI_4^{2-} layer in the new 2D crystals with conjugated ligands because of their structural similarity. The highest occupied molecular orbital (HOMO) energy levels of 4Tm, **4TCNm** and **BTm** were measured to be -5.28 eV, -6.07 eV and -5.58 eV, respectively. The HOMO energy level of **4Tm** was cross-checked using both UPS and CV methods (see Supplementary Fig. 14, 15 and related discussion). Next, the conduction band minimum (CBM) and the lowest unoccupied molecular orbital (LUMO) energy levels were calculated based on their optical bandgaps. We depicted qualitative band alignments for these hybrid 2D crystals (Fig. 2d). Note, the key assumption is that the inorganic layers have similar energy levels for all these compounds because they show similar structure and tilting (Fig. 1b-1e, Supplementary Fig. 2-4 and 10). To further verify this assumption and better depict the band alignments, all-electron hybrid density functional theory calculations in the FHI-aims code[43,44] were performed to calculate the complete electronic structures and frontier orbitals of the isolated organic molecules, as well as of crystalline $(BA)_2PbI_4$, $(2T)_2PbI_4$ and $(BTm)_2PbI_4$ (see Supplementary Fig. 16-18 and Supplementary Table 5). The geometric structure and, importantly, the predicted energy level positions agree well with the experimental trends. For structures of the size and complexity studied here, the level of theory used is already rather demanding. It would also be desirable to computationally address excitonic phenomena, as can now be done for somewhat smaller 2D perovskites[45], but an unbiased many-body theory treatment of excitons in the larger unit cells considered in this work remains as yet out of reach[45].

The energy and charge transfer processes were further characterized via time- and spectral-resolved PL spectroscopy using a streak camera with a time resolution of ~ 2 ps (Fig.3). All the active components except for **2T** can be excited by the excitation wavelength of 400 nm (3.1 eV). Because the band gap **2T** molecules is larger than 3.1 eV, the PL decay of $(2T)_2PbI_4$ reflects only the exciton dynamics of the inorganic layer (PbI_4^{2-}). We note that the PL decay includes both radiative and nonradiative pathways. As shown in Fig. 3a, b, and c, the decrease of PL lifetime in $(4Tm)_2PbI_4$ and $(4TCNm)_2PbI_4$ and the significant quenching of the PL intensity in comparison with $(2T)_2PbI_4$ is consistent with their type II band alignment that allows charge transfer at the interface. The charge transfer time can be estimated from the fast component of the PL decay by monitoring the emission from PbI_4 within the spectral range of 490-530 nm, which is determined to be 3.8 ± 0.2 and 4.3 ± 0.3 ps for $(4Tm)_2PbI_4$ and $(4TCNm)_2PbI_4$, respectively (Fig. 3e). The charge transfer time at the organic-inorganic interface in these 2D perovskites is similar to that at the tetracene/WS_2 interface[42]. For $(BTm)_2PbI_4$, the emission from the inorganic layer is almost entirely quenched and only emission from **BTm** is observed. This observation can be explained by energy transfer from the inorganic layer to **BTm**. We cannot determine the energy transfer time because it is faster than the time resolution of ~ 2 ps of our experiments. While it is possible that the difference in defect density for the samples could lead to different PL lifetimes, but we rule out this possibility because the defect density is similarly low, $< 10^{14}$ cm^{-3} (supplementary Fig. 19). The efficient energy/charge transfer processes with characteristic time on the picosecond timescale suggest great potentials for applications in efficient solid-state lightings and high gain photodetectors.

Materials stability

The large conjugated ligands are not only essential to tune the crystal morphology and electronic properties, but also helpful to improve the stability of the halide perovskites. We found that the new perovskite quantum wells are very stable even under harsh conditions (e.g., under water or during heating). Fig. 4a shows PL image of the samples under UV light illumination before and after immersion in water. $(BA)_2PbI_4$ degraded and their PL disappeared immediately when coming into contact with water. The green PL of $(2T)_2PbI_4$ was retained for about one minute and then started to degrade. $(4Tm)_2PbI_4$, $(4TCNm)_2PbI_4$, and $(BTm)_2PbI_4$ show no sign of decomposition after 5 minutes in water (Fig. 4b). They also exhibit excellent thermal stability, showing no signs of decomposition up to 250 ^{o}C (Supplementary Fig. 20). The origin of this enhanced stability was investigated using molecular dynamics simulations of $(BA)_2PbI_4$, $(2T)_2PbI_4$, and $(BTm)_2PbI_4$ with direct immersion in water. In the simulations, the films were initially dehydrated and allowed to equilibrate with bulk water over 2 ns. Supplementary Fig. 21 summarizes the quantitative distribution of water molecules around the perovskites. It was found that water penetrates the $(BA)_2PbI_4$ organic layer and completely dissolves the surface cations within 2 ns (Fig. 4c). The intermediate case of $(2T)_2PbI_4$ exhibits partial penetration of water into the organic layer via dissolution of some surface cations and the formation of well-defined channels (Fig. 4d). Interestingly, the $(BT)_2PbI_4$ film exhibits minimal water penetration into the upper organic layer and the inorganic surface remains dehydrated (Fig. 4e, also see Supplementary Fig. 22 for a complete configuration). Based on the experimental results and simulations, we conclude that water penetration accompanied by cation dissolution is the primary mechanism of decomposition. The bulky and hydrophobic organic conjugated groups were able to provide better protection to the perovskites and did significantly enhance their environmental stability. Finally, molecular dynamics simulations were also used to predict the observed crystal packing and disorder and the results matches very well with the experimental X-ray crystal structures (see discussions in Supplementary Fig. 23 and Supplementary Table 6).

In summary, we have demonstrated that the organic and inorganic building blocks of hybrid perovskite materials can be manipulated in a modular fashion to produce widely-tunable single-crystalline quantum wells. The overall optical and electronic properties are determined by the interaction of these two components. The materials' design and synthesis strategy presented here could serve as a blueprint for many other functional complex organic molecules. We anticipate that this work will lead to further studies on the chemistry and physics of 2D hybrid perovskite single and multiple quantum wells for the preparation of materials with properties suitable for example for light harvesting, light emission, and charge transport. We hope that other molecularly engineered solution-processed semiconductors quantum wells with high intrinsic stability can be developed that would serve as functional materials in fields such as nanoelectronics, optoelectronics, and photonics.

Data availability

Crystallographic data for the structures reported in this Article have been deposited at the Cambridge Crystallographic Data Centre, under deposition numbers CCDC 1846391 [$(4Tm)_2PbI_4$], 1846392 [$(BTm)_2PbI_4$] and 1861843 [$(2T)_2PbI_4$]. Copies of the data can be obtained free of charge via https://www.ccdc.cam.ac.uk/structures/. All other data supporting the findings of this study are available within the Article and its Supplementary Information, or from the corresponding author upon reasonable request.

References and notes

1 Levine, B. F. Quantum-well infrared photodetectors. *J. Appl. Phys.* **74**, R1-R81 (1993).

2 Shuji, N. *et al.* InGaN-Based Multi-Quantum-Well-Structure Laser Diodes. *Jpn. J. Appl. Phys.* **35**, L74 (1996).

3 Hicks, L. D. & Dresselhaus, M. S. Effect of quantum-well structures on the thermoelectric figure of merit. *Physical Review B* **47**, 12727-12731 (1993).

4 Ishihara, T., Takahashi, J. & Goto, T. Exciton state in two-dimensional perovskite semiconductor $(C_{10}H_{21}NH_3)_2PbI_4$. *Solid State Commun.* **69**, 933-936 (1989).

5 Meresse, A. & Daoud, A. Bis(*n*-propylammonium) tetrachloroplumbate. *Acta Crystallographica Section C* **45**, 194-196 (1989).

6 Mitzi, D. B., Feild, C. A., Harrison, W. T. A. & Guloy, A. M. Conducting tin halides with a layered organic-based perovskite structure. *Nature* **369**, 467 (1994).

7 Mitzi, D. B., Wang, S., Feild, C. A., Chess, C. A. & Guloy, A. M. Conducting Layered Organic-inorganic Halides Containing <110>-Oriented Perovskite Sheets. *Science* **267**, 1473-1476 (1995).

8 Papavassiliou, G. C. Three- and low-dimensional inorganic semiconductors. *Prog. Solid State Chem.* **25**, 125-270 (1997).

9 Kagan, C. R., Mitzi, D. B. & Dimitrakopoulos, C. D. Organic-Inorganic Hybrid Materials as Semiconducting Channels in Thin-Film Field-Effect Transistors. *Science* **286**, 945-947 (1999).

10 Borriello, I., Cantele, G. & Ninno, D. Ab initioinvestigation of hybrid organic-inorganic perovskites based on tin halides. *Physical Review B* **77**, 235214 (2008).

11 Lanty, G. *et al.* Room-Temperature Optical Tunability and Inhomogeneous Broadening in 2D-Layered Organic-Inorganic Perovskite Pseudobinary Alloys. *J. Phys. Chem. Lett.* **5**, 3958-3963 (2014).

12 Smith, I. C., Hoke, E. T., Solis-Ibarra, D., McGehee, M. D. & Karunadasa, H. I. A Layered Hybrid Perovskite Solar-Cell Absorber with Enhanced Moisture Stability. *Angew. Chem. Int. Ed.* **53**, 11232-11235 (2014).

13 Dou, L. T. *et al.* Atomically thin two-dimensional organic-inorganic hybrid perovskites. *Science* **349**, 1518-1521 (2015).

14 Ha, S. T., Shen, C., Zhang, J. & Xiong, Q. H. Laser cooling of organic-inorganic lead halide perovskites. *Nat. Photonics* **10**, 115-121 (2016).

15 Stoumpos, C. C. *et al.* Ruddlesden-Popper Hybrid Lead Iodide Perovskite 2D Homologous Semiconductors. *Chem. Mater.* **28**, 2852-2867 (2016).

16 Tsai, H. *et al.* High-efficiency two-dimensional Ruddlesden-Popper perovskite solar cells. *Nature* **536**, 312-316 (2016).

17 Wang, N. *et al.* Perovskite light-emitting diodes based on solution-processed self-organized multiple quantum wells. *Nat. Photonics* **10**, 699-704 (2016).

18 Yuan, M. *et al.* Perovskite energy funnels for efficient light-emitting diodes. *Nat. Nanotechnol.* **11**, 872-877 (2016).

19 Mao, L. L. *et al.* Tunable White-Light Emission in Single-Cation-Templated Three-Layered 2D Perovskites $(CH_3CH_2NH_3)_4Pb_3Br_{10-x}Cl_x$. *J. Am. Chem. Soc.* **139**, 11956-11963 (2017).

20 Proppe, A. H. *et al.* Synthetic Control over Quantum Well Width Distribution and Carrier Migration in Low-Dimensional Perovskite Photovoltaics. *J. Am. Chem. Soc.* **140**, 2890-2896 (2018).

21 Shi, E. *et al.* Two-dimensional halide perovskite nanomaterials and heterostructures. *Chem. Soc. Rev.* 10.1039/C7CS00886D (2018).

22 Mitzi, D. B. Templating and structural engineering in organic–inorganic perovskites. *J. Chem. Soc., Dalton Trans.* **0**, 1-12 (2001).

23 Saparov, B. & Mitzi, D. B. Organic-Inorganic Perovskites: Structural Versatility for Functional Materials Design. *Chem. Rev.* **116**, 4558-4596 (2016).

24 Braun, M., Tuffentsammer, W., Wachtel, H. & Wolf, H. C. Pyrene as emitting chromophore in organic-inorganic lead halide-based layered perovskites with different halides. *Chem. Phys. Lett.* **307**, 373-378 (1999).

25 Chondroudis, K. & Mitzi, D. B. Electroluminescence from an organic-inorganic perovskite incorporating a quaterthiophene dye within lead halide perovskite layers. *Chem. Mater.* **11**, 3028-3030 (1999).

26 Mitzi, D. B., Chondroudis, K. & Kagan, C. R. Design, structure, and optical properties of organic-inorganic perovskites containing an oligothiophene chromophore. *Inorg. Chem.* **38**, 6246-6256 (1999).

27 Takeoka, Y., Asai, K., Rikukawa, M. & Sanui, K. Incorporation of conjugated polydiacetylene systems into organic-inorganic quantum-well structures. *Chem. Commun.* , 2592-2593 (2001).

28 Zhu, X. H. *et al.* Effect of mono- versus di-ammonium cation of 2,2 '-bithiophene derivatives on the structure of organic-inorganic hybrid materials based on iodo metallates. *Inorg. Chem.* **42**, 5330-5339 (2003).

29 Ema, K., Inomata, M., Kato, Y., Kunugita, H. & Era, M. Nearly perfect triplet-triplet energy transfer from Wannier excitons to naphthalene in organic-inorganic hybrid quantum-well materials. *Phys. Rev. Lett.* **100**, 257401 (2008).

30 Era, M., Kobayashi, T., Sakaguchi, K., Tsukamoto, E. & Oishi, Y. Electric conduction of PbBr-based layered perovskite organic–inorganic superlattice having carbazole chromophore-linked ammonium molecule as an organic layer. *Org. Electron.* **14**, 1313-1317 (2013).

31 Papavassiliou, G. C., Mousdis, G. A., Pagona, G., Karousis, N. & Vidali, M.-S. Room temperature enhanced blue-green, yellow-orange and red phosphorescence from some

compounds of the type $(CH_3NH_3)_{n-1}$(1-naphthylmethyl ammonium)$_2Pb_n(Cl_xBr_{1-x})_{3n+1}$ (with n=1, 2 and $0 \leq x \leq 1$) and related observations from similar compounds. *J. Lumin.* **149**, 287-291 (2014).

32 Evans, H. A. *et al.* (TTF)Pb_2I_5: A Radical Cation-Stabilized Hybrid Lead Iodide with Synergistic Optoelectronic Signatures. *Chem. Mater.* **28**, 3607-3611 (2016).

33 Cortecchia, D., Soci, C., Cametti, M., Petrozza, A. & Marti-Rujas, J. Crystal Engineering of a Two-Dimensional Lead-Free Perovskite with Functional Organic Cations by Second-Sphere Coordination. *Chempluschem* **82**, 681-685 (2017).

34 Du, K. Z. *et al.* Two-Dimensional Lead(II) Halide-Based Hybrid Perovskites Templated by Acene Alkylamines: Crystal Structures, Optical Properties, and Piezoelectricity. *Inorg. Chem.* **56**, 9291-9302 (2017).

35 Ortiz-Cervantes, C., Román-Román, P. I., Vazquez-Chavez, J., Hernández-Rodríguez, M. & Solis-Ibarra, D. Thousand-fold Conductivity Increase in 2D Perovskites by Polydiacetylene Incorporation and Doping. *Angew. Chem. Int. Ed.* **57**, 13882-13886 (2018).

36 Passarelli, J. V. *et al.* Enhanced Out-of-Plane Conductivity and Photovoltaic Performance in n = 1 Layered Perovskites through Organic Cation Design. *J. Am. Chem. Soc.* **140**, 7313-7323 (2018).

37 Mitzi, D. B. *Chem. Mater.* **8**, 791-800 (1996).

38 Billing, D. G. & Lemmerer, A. *Acta Crystallogr.,Sect.B* **63**, 735-747 (2007).

39 Liao, W.-Q. *et al.* A lead-halide perovskite molecular ferroelectric semiconductor. *Nat. Commun.* **6**, 7338 (2015).

40 Niu, W., Eiden, A., Vijaya Prakash, G. & Baumberg, J. J. Exfoliation of self-assembled 2D organic-inorganic perovskite semiconductors. *Appl. Phys. Lett.* **104**, 171111 (2014).

41 Straus, D. B. & Kagan, C. R. Electrons, Excitons, and Phonons in Two-Dimensional Hybrid Perovskites: Connecting Structural, Optical, and Electronic Properties. *J. Phys. Chem. Lett.* **9**, 1434-1447 (2018).

42 Zhu, T. *et al.* Highly mobile charge-transfer excitons in two-dimensional WS_2/tetracene heterostructures. *Sci. Adv.* **4**, eaao3104 (2018).

43 Blum, V. *et al.* Ab initio molecular simulations with numeric atom-centered orbitals. *Comput. Phys. Commun.* **180**, 2175-2196 (2009).

44 Liu, C. *et al.* Tunable Semiconductors: Control over Carrier States and Excitations in Layered Hybrid Organic-Inorganic Perovskites. *Phys. Rev. Lett.* **121**, 146401 (2018).

45 Leveillee, J. *et al.* Influence of π-conjugated cations and halogen substitution on the optoelectronic and excitonic properties of layered hybrid perovskites. *Phys. Rev. Materials* **2**, 105406 (2018).

Acknowledgements

This work is supported by the US Office of Naval Research (award to L.D.; N00014-19-1-2296, Program Manager: Paul Armistead), and Davidson School of Chemical Engineering, College of Engineering, and Birck Nanotechnology Center of Purdue University. L.H., J.S, and S.D acknowledge the support from US Department of Energy, Office of Basic Energy Sciences through award DE-SC0016356. B.W.B. acknowledges the support from Air Force Office of Scientific Research (FA9550-15-1-0449). The work on the single crystal X-ray diffractions was supported by the National Science Foundation (CHE 1625543). V.B. and R.S. acknowledge research supported as part of the Center for Hybrid Organic Inorganic Semiconductors for Energy (CHOISE), an Energy Frontier Research Center funded by the U. S. Department of Energy, Office of Science, Basic Energy Sciences (BES). An award of computer time was provided by the INCITE program. This research used resources of the Argonne Leadership Computing Facility, which is a DOE Office of Science User Facility supported under Contract DE-AC02-06CH11357. S.J. thanks the Deutsche Forschungsgemeinschaft (DFG, Ger-man Research Foundation) for a postdoctoral fellowship (393196393). TEM work is supported by the Center for High-resolution Electron Microscopy (CħEM) at ShanghaiTech University. The authors thank G. Wiederrecht and R. Schaller for assistance in the streak camera measurements; D. Zemlyanov for the UPS measurements; D. Kumar for GIWAXS data processing (Xi-Cam); J. Mei for CV measurements; and S. Beaudoin for AFM measurements.

Author contributions

L.D. conceived the idea and supervised the project. Y.G. carried out the materials synthesis, structural characterizations, and data analysis. E.S. synthesized the nanocrystals. J.S., S.D. and L.H. carried out the ultrafast spectroscopy measurements and data analysis. S.B.S. and B.S. performed molecular dynamics simulations. C.L., B.Y. and Y.Y. carried out HRTEM measurements and data analysis. A.L.-P. and C.Z. carried out GIWAXS measurements. P.Y., P.L., R.S., S.J. and V.B. performed DFT simulations. M.Z. collected single crystal X-ray data and solved and refined the crystal structures. B.W.B. provided characterization facilities and participated data analysis and manuscript preparation. Y.G. and L.D. wrote the manuscript. All authors discussed the results and revised the manuscript.

Additional information

Reprints and permissions information is available online at www.nature.com/reprints. Correspondence and requests for materials should be addressed to L.D.

Competing interests

The authors declare no competing interests.

Figure 1| Structures of the conjugated organic ligands and 2D hybrid perovskites. a, Chemical structures of the conjugated organic ligands investigated in this study, which feature a mono-ammonium end group. Sterically more demanding methyl groups are represented by pink circles. **b**, Side view of the crystal structure of a $(BA)_2PbI_4$ sheet. **c**, Side view of the crystal structure of a $(2T)_2PbI_4$ sheet. **d**, Side view of the crystal structure of a $(4Tm)_2PbI_4$ sheet. **e**, Side view of the crystal structure of a $(BTm)_2PbI_4$ sheet. Colour code: I, purple; S, yellow; N, blue; C, grey; blue diamonds within inorganic layers represent $[PbI_6]^{4-}$ octahedral; hydrogen atoms are omitted for clarity.

Figure 2| Optical properties of the hybrid halide perovskites quantum wells. a, Optical microscopy images of the assembled 2D crystals grown on SiO_2/Si substrates: $(2T)_2PbI_4$ (i), $(4Tm)_2PbI_4$ (ii), $(4TCNm)_2PbI_4$ (iii), $(BTm)_2PbI_4$ (iv). All scale bars are 10 μm. The insets are images for mono-layer thick single quantum well structures. All scale bars in the insets are 5 μm. **b**, Corresponding PL image of the assembled 2D crystals under UV excitation. All scale bars are 10 μm. The insets are the PL images for the corresponding mono-layer thick single quantum well structures. All scale bars in the insets are 5 μm. **c**, Corresponding steady state PL spectra of the mono-layers (red curves), bulk crystals (dark red curves). In c(i) inset, $(BA)_2PbI_4$ mono-layers (grey solid curves) and bulk crystals (grey dashed curves) are shown for comparison. In c(ii) and c(iii) insets, the PL for the **4Tm** and **4TCNm** ligands (blue curves) are shown for comparison. It can be seen that the PL for both organic and inorganic layers is quenched and only very weak signals are observed. **d**, Corresponding energy level alignments (relative energy levels) of organic (dark-red lines) and inorganic (dark-blue lines) layers within the hybrid 2D perovskites: $(2T)_2PbI_4$ (i), $(4Tm)_2PbI_4$ (ii), $(4TCNm)_2PbI_4$ (iii), $(BTm)_2PbI_4$ (iv).

Figure 3| Time- and spectral-resolved PL spectroscopy. a-d, Temporal and spectral dependent PL intensity of $(2T)_2PbI_4$ (a), $(4Tm)_2PbI_4$ (b), $(4TCNm)_2PbI_4$ (c) and $(BTm)_2PbI_4$ (d), excited at 400 nm and recorded by a streak camera. **e**, The PL decay curves integrated from 490 nm to 530 nm for $(2T)_2PbI_4$, $(4Tm)_2PbI_4$, $(4TCNm)_2PbI_4$ are shown for comparison. The time constants of fast decay process are determined to be 29.0 ± 0.3, 3.8 ± 0.2 and 4.3 ± 0.3 ps respectively. Because there is no any signal detected from 490 nm to 530 nm for $(BTm)_2PbI_4$, the energy transfer time from **BTm** to the inorganic layer cannot be determined.

Figure 4| Stability of hybrid halide perovskite quantum wells. a, Photos of 2D hybrid halide perovskite thin films with different organic ligands under UV lamp irradiation before (top) and after (bottom) immersion in water. From left to right: $(BA)_2PbI_4$, $(2T)_2PbI_4$, $(4Tm)_2PbI_4$,

$(4TCNm)_2PbI_4$, $(BTm)_2PbI_4$. **b**, XRD profiles of the corresponding compounds after water treatments. **c-e**, Snapshots from the molecular dynamics simulations for $(BA)_2PbI_4$ (c), $(2T)_2PbI_4$ (d), and $(BTm)_2PbI_4$ (e), showing a 2 nm cross-section of each perovskite layer after 1 ns of equilibration. The scale bars are 1 nm. For clarity, these images focus on the inorganic layers and only part of the organic ligands are shown.

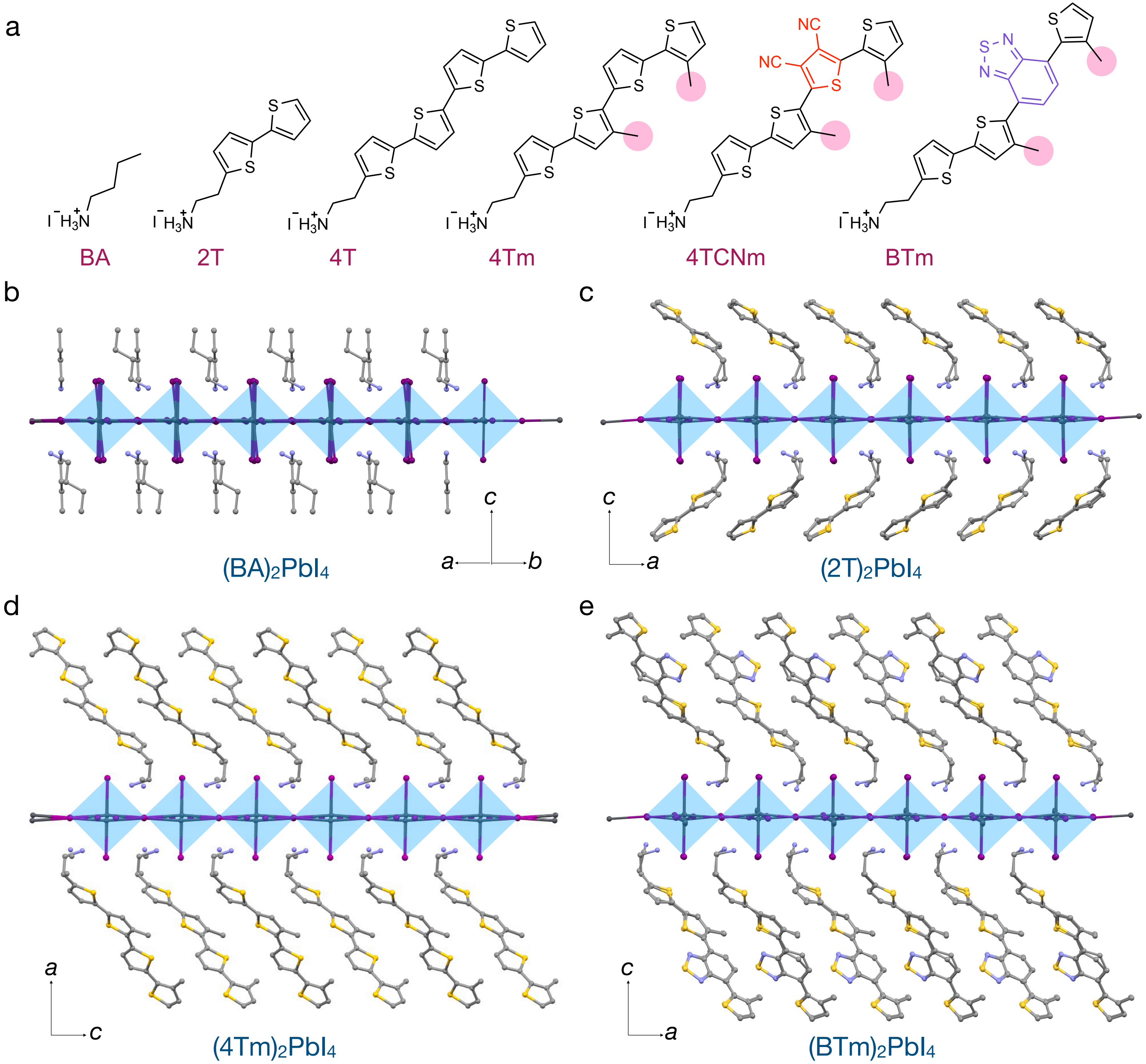
a
I⁻ H3N⁺
S
NC
N
BA
2T
4T
4Tm
4TCNm
BTm
b
c
a
b
c
(BA)2PbI4
c
a
(2T)2PbI4
d
a
c
(4Tm)2PbI4
e
c
a
(BTm)2PbI4

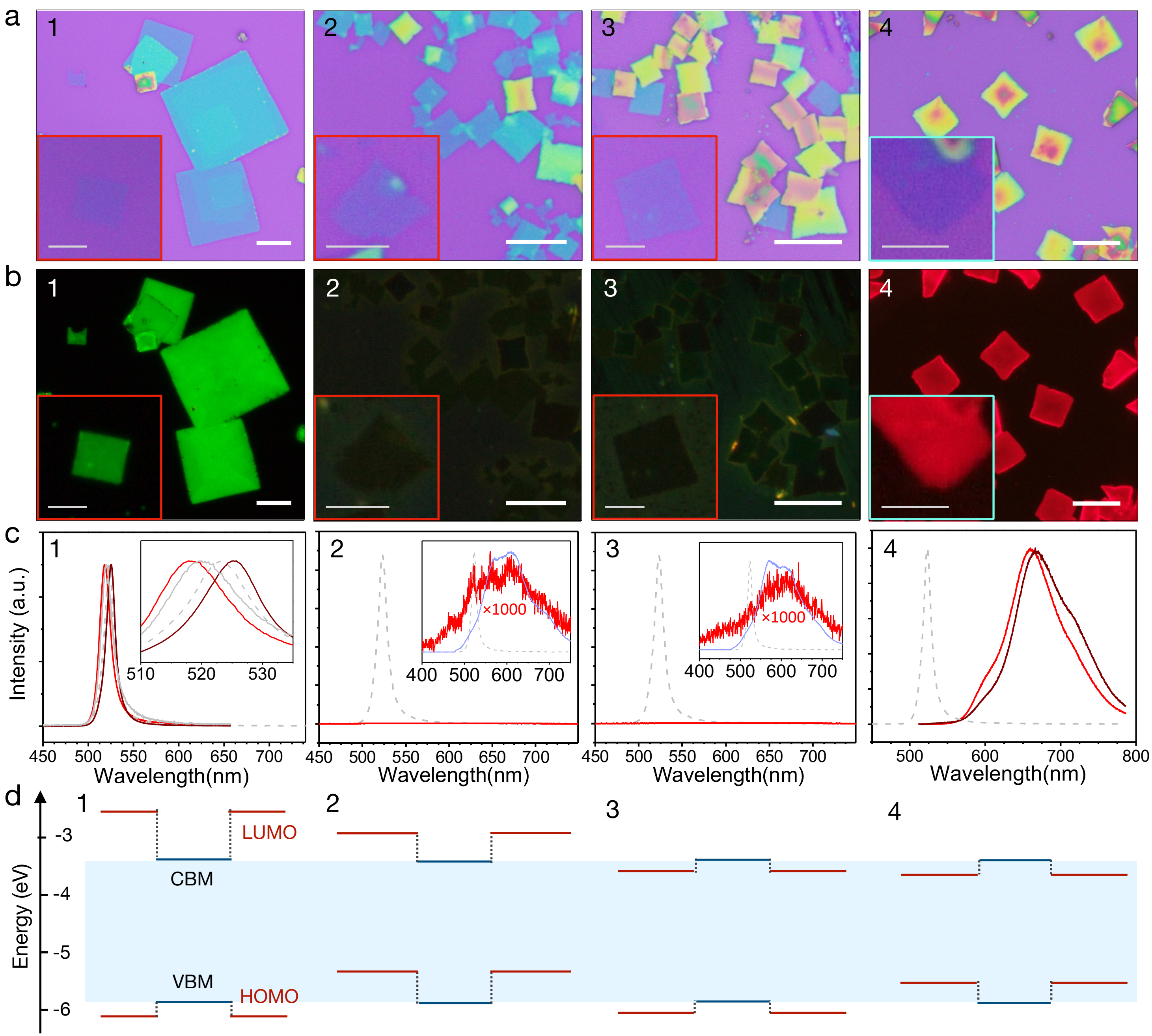
a
1
2
3
4
b
1
2
3
4
c
1
2
3
4
Intensity (a.u.)
510
520
530
×1000
400
500
600
700
450
500
550
600
650
700
800
Wavelength(nm)
d
Energy (eV)
-3
-4
-5
-6
LUMO
CBM
VBM
HOMO

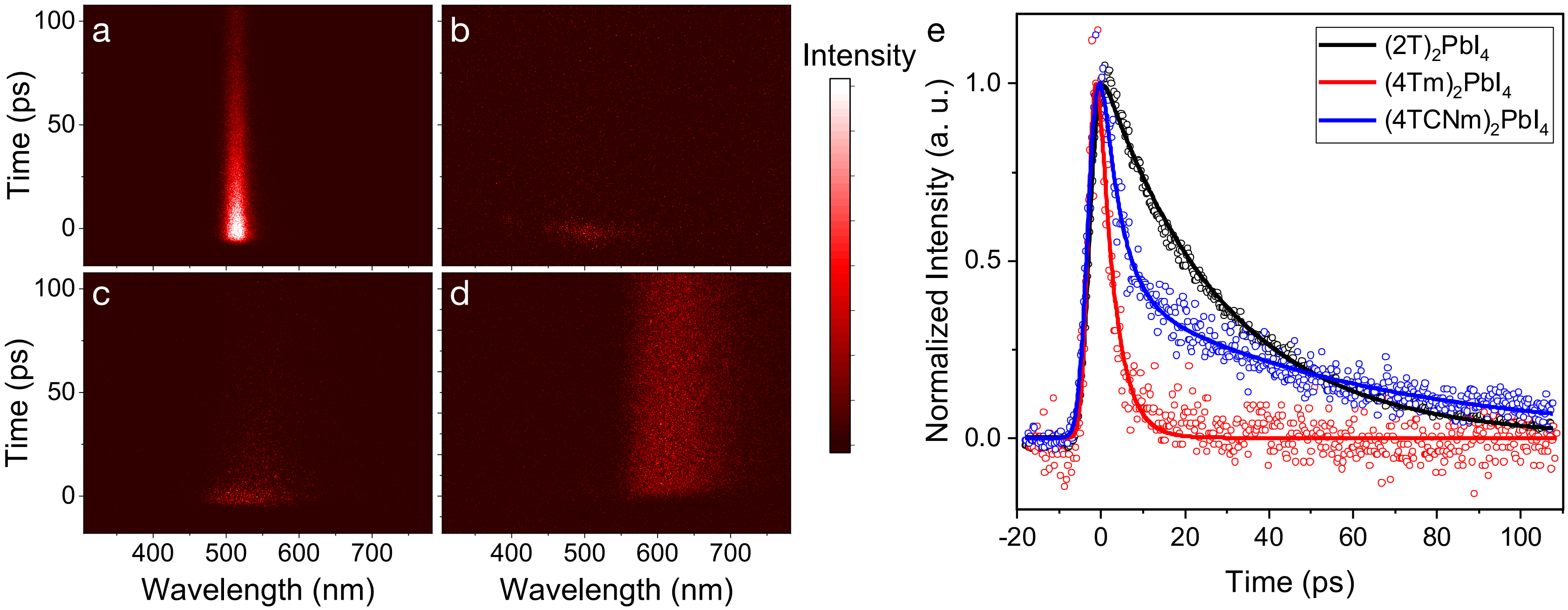
a
b
c
d
e
Time (ps)
100
50
0
Wavelength (nm)
400
500
600
700
Intensity
Normalized Intensity (a. u.)
1.0
0.5
0.0
Time (ps)
-20
0
20
40
60
80
100
$(2T)_2PbI_4$
$(4Tm)_2PbI_4$
$(4TCNm)_2PbI_4$

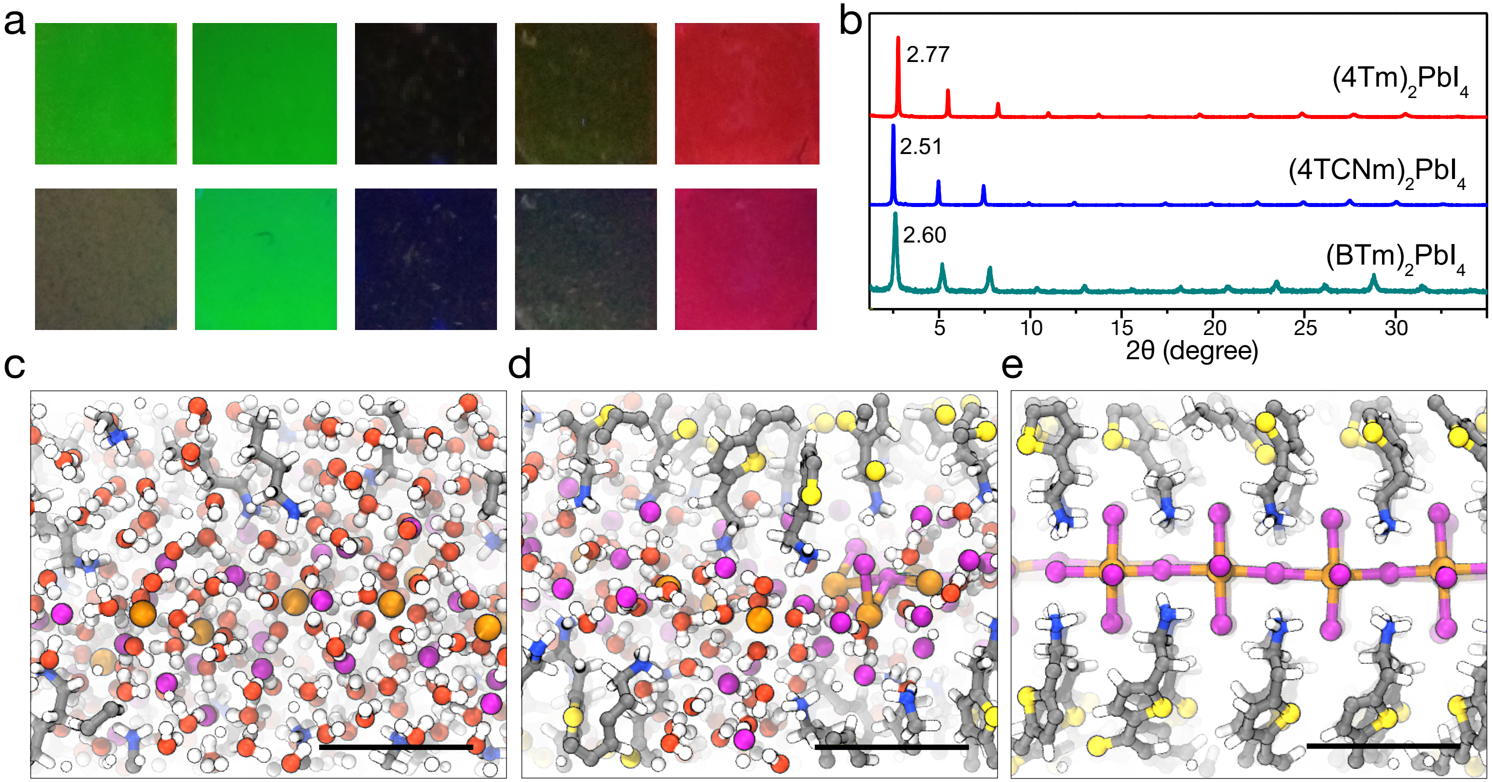

$(BA)_2PbI_4$ $(2T)_2PbI_4$ $(BTm)_2PbI_4$

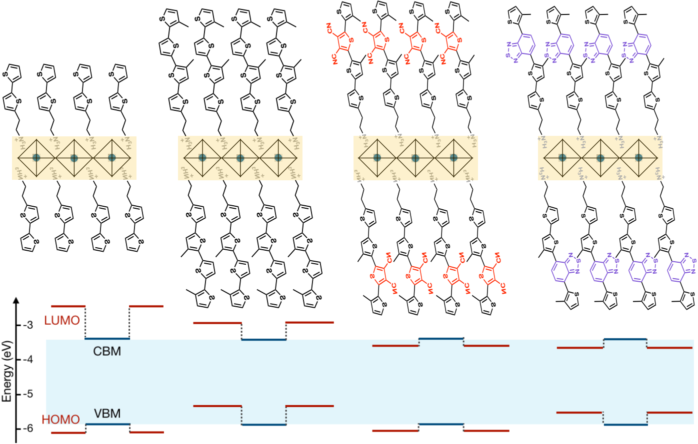

LUMO
CBM
VBM
HOMO
Energy (eV)
-3
-4
-5
-6
H_3N^+
S
NC
CN
N